Publications of the Astronomical Society of the Pacific
109: 307–318, 1997 March

Hertz, a Submillimeter Polarimeter

D. A. Schleuning,[1,2,3] C. D. Dowell,[1,2,3] R. H. Hildebrand,[1,2,3,4] and S. R. Platt[1,2,3]

The University of Chicago, 5640 S. Ellis Avenue, Chicago, Illinois 60637
Electronic mail: david@oddjob.uchicago.edu, cdd@oddjob.uchicago.edu, roger@oddjob.uchicago.edu, srp@hale.yerkes.uchicago.edu

G. Novak

Department of Physics and Astronomy, Dearborn Observatory, Northwestern University, Evanston, Illinois 60208-2900
Electronic mail: g-novak@nwu.edu

Received 1996 July 18; accepted 1996 November 22

ABSTRACT. We describe a 32 pixel polarimeter, Hertz, for use at the Caltech Submillimeter Observatory. We present polarization maps of the Orion molecular cloud (OMC-1) at 350 μm (46 detections) and 450 μm (19 detections) with 3σ or better statistical significance. The 350 μm polarization ranges from 1.4% to 6.8% with a median value of 3.3%. The position angles are fairly uniform across the source at an angle of $\sim$30 degrees (east of north). We describe the design and performance characteristics of the polarimeter and discuss systematic effects due to telescope and instrumental polarization, atmospheric fluctuations, and reference beam flux.

1. INTRODUCTION

The University of Chicago polarimeter, Hertz, is designed to make polarimetric images in the submillimeter (λ=350 μm) from the Caltech Submillimeter Observatory (CSO). The instrument simultaneously maps the polarized and total flux density with 18″ resolution using two 32-detector arrays to measure orthogonal components of linear polarization.

Extended maps of polarization allow one to investigate magnetic fields and to constrain fundamental properties of dust grains. For grains aligned by the magnetic field, the submillimeter polarization will be perpendicular to the magnetic field in the plane of the sky. The magnitude of the polarization will depend on grain properties, alignment efficiency, and uniformity of the magnetic field along the line of sight (Hildebrand 1988).

Previous studies in the far infrared (λ=100 μm) used an airborne instrument to make some 600 detections of polarized emission from nine molecular clouds (Hildebrand et al. 1995; Dotson 1996; Novak et al. 1997) as well as several regions near the Galactic center (Hildebrand et al. 1993; Morris et al. 1992). These studies have shown measurable polarization in every observed cloud and smooth magnetic-field morphologies. The polarization is typically low (median value $\sim$3%) and shows a trend of reduced polarization with increasing optical depth. This empirical trend has also been observed in the submillimeter (450 μm: Schleuning et al. 1996; 800 μm: Minchin and Murray 1994) and millimeter (1.3 mm: Leach et al. 1991) wavelengths and has the consequence of low polarization at flux peaks. The trend also implies that the polarized flux in extended regions drops off less rapidly than the total flux.

[1]Enrico Fermi Institute.
[2]Department of Astronomy and Astrophysics.
[3]Yerkes Observatory.
[4]Department of Physics.

Submillimeter polarimetry will complement measurements at shorter wavelengths from airborne observatories (KAO and SOFIA) and space missions (ISO and PIREX) by sampling different grain environments. While far-infrared measurements favor warm dust near heating sources, submillimeter measurements favor higher column densities in cooler regions. Polarimetry of the cooler dust is better matched to OH Zeeman measurements which give the line-of-sight strength of the magnetic field.

In Sec. 2, we describe the design and performance of the polarimeter. In Sec. 3, we estimate systematic effects and discuss their removal from the data where possible. In Sec. 4, we present results for the Orion Molecular Cloud (OMC-1).

2. DESCRIPTION OF THE INSTRUMENT

Hertz incorporates many of the design features of the far-infrared polarimeter, Stokes, described by Platt et al. (1991). A schematic drawing is shown in Fig. 1. Optics specifications are given in Table 1. In both instruments, silicon bolometers are cooled by a two-stage ^{3}He refrigerator to an operating temperature of 300 mK. We employ fast chopping (3 Hz) of the secondary mirror to remove the high sky background and slow beam switching (0.1 Hz) to remove offsets. The half-wave plate (HWP) is stepped slowly to measure the polarization signal. In this section, we describe the optical, cryogenic, and electrical design of Hertz. We also present the measured sensitivity and describe future improvements for better performance.

2.1 Optical Design

The optical design of Hertz makes a balance between throughput and resolution. We have chosen 18″ beams ($\lambda^{-2}\int A\, d\Omega$=2.5) to increase the throughput of the optics while maintaining resolution near the diffraction limit.

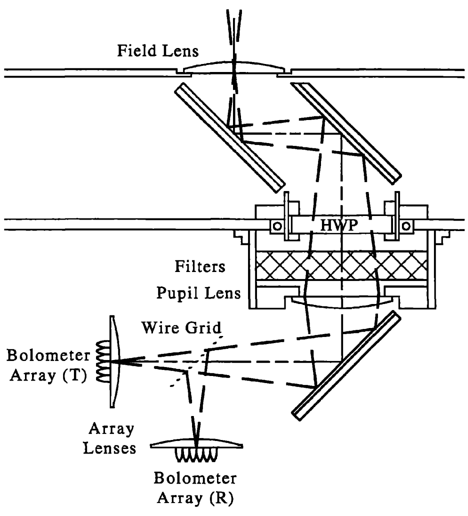

FIG. 1—Schematic diagram of the optical design of Hertz. All of the optical elements are attached to the ^{4}He surface, except for the arrays, which are connected to the ^{3}He cold surface. Dashed lines trace the beam for a Winston cone at the center of the focal plane. The field lens at the telescope focal plane reimages the primary onto the pupil lens. Near the pupil, the half-wave plate (HWP) rotates the plane of polarization. Filters block all but the 350 μm broadband radiation ($\Delta\lambda/\lambda=0.1$). The pupil lens images the focal plane onto the arrays. A free-standing wire grid separates the orthogonal components of polarization. The lower array, shown schematically here, is oriented out of the page. The array lens directs the beam from each cone onto the pupil. The arrays each consist of Winston cones arranged in a 6×6 pattern with the corner cones omitted. Silicon bolometers are suspended behind each cone in a cylindrical cavity.

We have placed many of the optical elements near an image of the primary to reduce systematic polarization effects (Gonatas et al. 1989). The polyethylene pressure window is located at an image of the primary (14 cm in front of the focal plane). A field lens at the focal plane reimages the primary at a cold pupil stop. A rotating HWP as well as the pupil lens and filter assembly are mounted within 4 cm of the image of the primary. The filters and pupil lens are installed below the HWP, so that any induced linear polarization from these elements will not be a source of instrumental polarization. A free-standing wire grid splits the incoming beam into two planes of polarization. The grid mount can be adjusted cold to align the arrays on the sky with an accuracy of $<3''$ (20% of a beam). Measurements of Saturn give a beam spacing of $17.''6\pm0.''3$. A Gaussian fit to the beam has a FWHM of $18\pm3''$.

At the focal plane, Winston cones (Compound Parabolic Concentrators) concentrate the radiation into cylindrical cavities (Hildebrand 1986). A polyethylene lens is mounted in front of each array so that beams emanating outward from all the cones are directed equally onto the pupil. Figure 2 illustrates the importance of an array lens in the fast optics of the CSO. The telescope's $f/4.48$ beam is reduced to an $f/3.90$ beam by the demagnification of the pupil lens. Without an array lens the acceptance beam for the Winston cones ($f/3.5$) off the dewar's optic axis will vignette the pupil stop, as can be seen in Fig. 2(a).

Consider rays emanating from a single point at the pupil. The array lens acts to tilt all these rays parallel to the ray that passes through the center of the lens. These rays will be equally rejected or accepted by Winston cones at the focal plane. Thus if the optic axis through the pupil lens is aligned with the center of the array lens, all pixels will equally see the image of the primary [Fig. 2(b)].

A resonant grid metal mesh filter made by Queen Mary College defines the passband at 350 μm ($\Delta\lambda/\lambda=0.1$). For initial observations in 1994, we used a similar 450 μm filter. Short-wavelength blocking is accomplished by a polyethylene pressure window with a diamond dust coating and by black polyethylene behind the HWP. Mid-infrared blocking is provided by the quartz lenses and HWP, which are opaque from 5 to 40 μm. The passband is 36 μm ($\Delta\nu=90$ GHz). The optical transmission of the dewar is 23%. To calculate the total transmission, one must also consider the point-source efficiency of the telescope (20%–30%), the atmospheric transmission (~30%), and the coupling constant of the detectors (2%–6%). We define the coupling constant (α) of the detectors as the ratio of the measured power to the calculated power emitted by a known source (lab and sky measurements), considering the transmission assumptions given above. The cause of this substantial loss could be due to poor absorption of the radiation by the detectors in the detector cavities, losses in the Winston cones, or other losses that are unaccounted in our optical transmission estimate.

The HWP is made of x-cut crystal quartz and is connected to the ^{4}He surface. A HWP of the incorrect thickness will reduce the polarization modulation efficiency (see Sec. 3.2). In our initial testing of the instrument we used a 6 mm HWP for operation at 450 μm, based on estimates of the indices of refraction for quartz at 1.5 K (Loewenstein et al. 1973). By observing a highly polarized source at various angles, we were able to determine an empirical value for the difference in indices of refraction (method outlined in the Appendix of Novak et al. 1989). We determine a value of $\Delta n=0.048$ ±0.002 for ^{4}He cooled quartz at submillimeter wavelengths, which is 25% greater than the value from Loewenstein et al. (1973) and in good agreement with more recent room-temperature measurements (Murray et al. 1992). This corresponds to thicknesses of 3.6 and 4.7 mm for 350 and 450 μm HWPs, respectively. For the 1995 observing run we installed a 3.6 mm HWP, improving the polarization modulation efficiency from 75% to 85%. The remaining inefficiency is most likely due to the polarizing grid.

2.2 Two-Stage ^{3}He Refrigerator

The Hertz cryostat is designed to have an operating temperature of 300 mK and to have hold times greater than 12 hr (the length of a typical night of observing) for the liquid nitrogen, ^{4}He, and ^{3}He stages. We have designed a mechanically rigid cold surface to support the field optics and electronics for the array. Figure 3 shows the layout of the ^{3}He stages and support structure. The guard stage acts to remove much of the conductive load from the ^{4}He surface. We have measured the equilibrium temperature of the cold stage as a function of applied heat and present empirical results with a model fit to the data. We have determined that the heat load

TABLE 1
Optics Specifications

	Quantity	Value	Units
CSO Telescope	Diameter	10.4	m
	F-ratio	4.48	
	Plate Scale	4.6	"/mm
Lengths	Focal Plane to Pupil	146	mm
	Pupil to Array	131	mm
Optics	Field Lens (Crystal Quartz)		
	Focal Length	73	mm
	Diameter	44	mm
	Pupil Lens (Crystal Quartz)		
	Focal Length	70	mm
	Diameter	44	mm
	Array Lens (Polyethylene)		
	Focal Length	132	mm
	Diameter	43	mm
	Winston Cones		
	Entrance Aperture	3.05	mm
	Exit Aperture	0.43	mm
	F-number	3.5	
Filter	Q.Mary College Metal Mesh		
	Resonant Grid Filter ($\Delta\lambda/\lambda$)	0.1	
HWP	X-cut Crystal Quartz	3.6	mm
Grids	Free-standing Gold-Coated (Dia.)	20	μm
	Tungsten Wire (spacing)	63	μm
Beam Size	Beam (FWHM)	18 ± 3	"
	Pixel Spacing	17.6 ± 0.3	"
Throughput	$\lambda^{-2}\int A\cdot d\Omega$	2.5	
	Transmission of Optics	23	%
	Detector Coupling Constant (α)	2-6	%
	Atmospheric Transmission (%)	~30	%
	Telescope Point Source Efficiency	20-30	%

is dominated by conduction along the G10 cylinders and straws (see Fig. 3) and that future reconfiguration could reduce the temperature to ~200 mK.

In an attempt to characterize the ^{3}He refrigerator, we tested the ^{3}He stages without the bolometer arrays, G10 straws, or manganin signal wires. We then added heat to the cold surface by applying current across a metal-film resistor. Heating with a constant power caused the cold surface to equilibrate at a higher temperature, which was measured with a calibrated germanium resistor (Lake Shore Cryotronics, Inc., Westerville, OH). The empirical results, shown in Fig. 4, give the dependence of equilibrium temperature on the heat load, which can be approximated as a power law ($T\sim\dot{Q}^{0.2}$).

To model the system we note that the pumped ^{3}He equilibrium temperature is determined by the vapor pressure above the ^{3}He liquid. This relationship (assuming a constant latent heat) is given by White (1993) and when fit to ^{3}He data (see Table A in the Appendix to White 1993) is given by the semiempirical form,

$$T=\frac{1.5\ \mathrm{K}}{2.32-\log(P_{\mathrm{vap}})}, \tag{1}$$

where P_{vap} is in mm Hg. The vapor pressure depends on the efficiency of the pumps, the impedance of the pump line, and the boiloff of the ^{3}He liquid. We assume that the boiloff from the ^{3}He plot is directly proportional to the heat load ($dN_{\mathrm{boil}}/dt\propto\dot{Q}$) and that the impedance of the line is negligible. The model does not include the effects of vapor cooling or convection currents in the ^{3}He gas which could have significant effects on the heat load, especially for high boiloff rates. The charcoal adsorption pumps will have an efficiency dependent on the surface area of the charcoal as well as the cooling power of the ^{4}He surface. We approximate the complicated function for the pump rate as $dN_{\mathrm{adsorption}}/dt\propto P^{1/n}$, where P is the vapor pressure at the pump. Combining these assumptions and Eq. (1), we derive a functional form for the equilibrium temperature given by

$$T_{\mathrm{equilibrium}}=\frac{1.5\ \mathrm{K}}{2.32-n\ \log(\epsilon\dot{Q})}, \tag{2}$$

where ϵ is a property of the cooling power and pump efficiency, $\dot{Q}$ is the heat load, and n is the inverse power law for the adsorption pumps. The dependence of equilibrium tem-

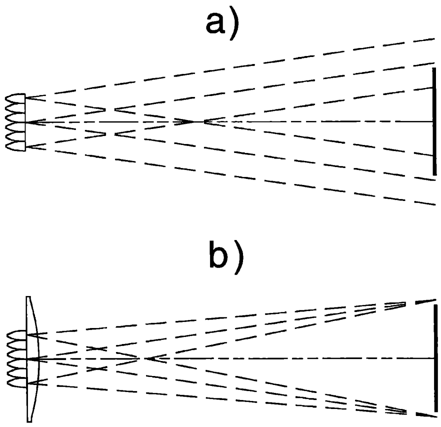

FIG. 2—Ray diagrams for Winston cones at the focal plane. The thick line to the right shows the size of the pupil. The dashed lines show schematic acceptance beams for cones at the focal plane. (a) Beams with no array lens at the focal plane. (b) Beams with an array lens at the focal plane. With an array lens, the beams from all the Winston cones equally illuminate the pupil.

perature on the heat load is shown in Fig. 4 [Eq. (2) and measured data].

Consider the guard stage which equilibrates at 350 mK without the G10 straws (Fig. 3). The calculated power from the ^{4}He surface through the G10 cylinders is 100 μW, which is in agreement with the power needed to raise the temperature to 350 mK estimated from Fig. 4. Adding the G10 straws and manganin wires, the temperature rises from 350 to 450 mK for the guard stage and from 180 to 300 mK for the cold stage. This additional load on the cold stage is most likely due to the G10 straws that may not be properly heat sunk to the guard stage. The calculated heat load from the manganin wires is negligible. Removing the straws would require completely rewiring the array, and providing alternate methods of support. However, with these improvements the system may be able to reach an equilibrium temperature of ~200 mK.

2.3 Detectors and Electronics

The two Hertz arrays have 32 bolometers each (a 6×6 pattern with the corners removed). A pair of bolometers, one from each array, forms one polarimetric pixel on the sky. Characteristics of the detectors are given in Table 2. The bolometers are chips of silicon doped with antimony and boron. The 13×16×6 mil (0.001 in) chips have been ion implanted and gold coated on their sides of lowest surface area. Half-mil brass leads are soldered to the gold-coated sides of the chips and connected to the cold bath.

We measure an electrical NEP of 1.0×10^{-15} W Hz^{-1} that is a combination of amplifier noise and thermal phonon noise. Due to the microphonic response inherent to high-impedance detectors, the NEP can be increased significantly by vibrations. Mechanical motion of the HWP induces such microphonics, thus limiting our observing strategy to integrating between movements of the HWP and waiting for the detectors to settle (typically a few seconds).

Each detector is individually wired from the array to an analog-to-digital converter. The high-impedance lines are current boosted by voltage follower JFETs. We find that our JFETs have a noisy regime between 80 and 100 K; therefore, the JFETs are weakly coupled to the liquid–nitrogen surface and heated to ~120 K. All 64 signals are separately preamplified and digitized with 16 bit resolution using a data system designed at NASA Goddard Space Flight Center (described by Wang et al. 1996). The digital signals are transferred over fiber optics to a DSP card in a Macintosh IIci computer which locks into the chopper wave form. The signal (in phase) and quadrature (out of phase) data are then stored in frames of eight chop cycles. Typical integrations consist of five frames at each of four beam-switched positions (left, right, right, left). A file consists of integrations at each of six HWP positions separated by 30 degrees. The entire file, including beam-switching, HWP movements, and settling time, takes 8 min of elapsed time, for 5 min and 20 s of integration time. The Macintosh computer communicates over an ethernet connection to the CSO antenna computer to beam switch the telescope, rotate the instrument, and record an observing log (e.g., telescope offsets, $\tau_{225\ \mathrm{GHz}}$, etc.) with each file.

2.4 Sensitivity

During an engineering run at the CSO in 1994 October, we tested Hertz and the newly installed chopping secondary and cassegrain relay optics. After modifications to the dewar and the telescope facility (including installation of an instrument rotator), we again observed with Hertz in Fall of 1995. Some of the characteristics and improvements are listed in Table 3.

To determine the sensitivity of the instrument we have made repeated measurements of Saturn at air masses ranging from 1.11 to 1.55 and in a variety of weather conditions, monitored with a radiometer at 225 GHz (τ_{225}~0.03–0.16). A fit to the data gave an NEFD of 20 Jy Hz$^{-1/2}$ during good weather conditions (τ_{225}=0.03). The performance falls exponentially as a function of airmass and τ_{225}. We estimate that "good" weather conditions only occur for about 20% of the nights.

In the far infrared (λ=100 μm), previous studies (Hildebrand et al. 1995) have found that typical thermal sources are weakly polarized (median value ~3%). Because sources are likely to have low polarization in the submillimeter, we characterize the sensitivity in terms of the desired precision of polarization measurements. We define a figure of merit,

$$T_{\mathrm{merit}}=\left(\frac{1}{\kappa}\right)\left(\frac{\sqrt{2}*\mathrm{NEFD}}{F_\nu \eta \sigma_p}\right)^2, \tag{3}$$

where κ is the duty cycle, F_ν is the photometric flux, η is the polarization modulation efficiency (see Sec. 3.2), σ_p is the polarization error, and T_{merit} is the elapsed time. We calculate a duty cycle (integration time divided by elapsed time) of 67%, which includes time for object setup, telescope beam switching, HWP movements, 90 degree instrument rotations, and computer crashes. For good weather conditions Hertz has a figure of merit of

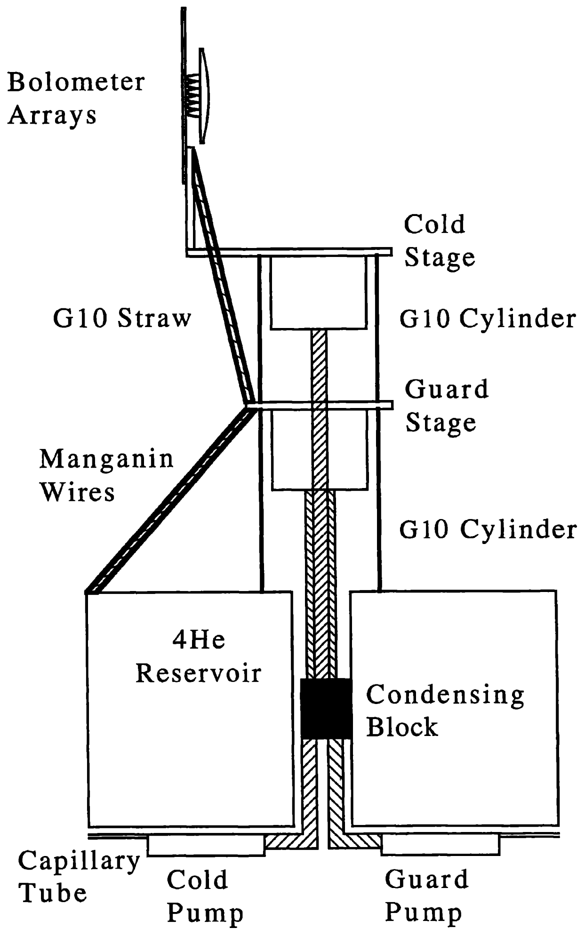

FIG. 3—Layout of the two-stage ^{3}He system. The self-contained ^{3}He system has exterior tanks (not shown) that connect to charcoal pumps by stainless-steel capillary tubes. The charcoal pumps are thermally isolated from the ^{4}He reservoir, but can be connected to it by mechanical heat switches. Stainless-steel bellows connect the pumps to a condensing block which is heat sunk to the ^{4}He reservoir. Coaxial bellows connect the condensing block to the ^{3}He pots. Mechanical integrity is achieved with thin (0.005 in) G10 cylinders which support the system above the ^{4}He surface. The arrays of Winston cones, heat traps, bolometers, and load resistors are supported off the cold stage by an aluminum mount and G10 straws. Manganin signal wires from the detector arrays are varnished to G10 straws, which are heat sunk to the guard stage and then connected to the ^{4}He surface.

$$T_{\rm merit}=5.1\ {\rm hr}\left(\frac{100\ {\rm Jy}}{F_\nu}\right)^2\left(\frac{0.3\%}{\sigma_p}\right)^2. \tag{4}$$

2.5 Future Improvements

Hertz is currently limited by the amplifier noise from the JFETs and the thermal phonon noise. Replacing the JFETs may lower the amplifier noise somewhat; however, a better method of improving the overall sensitivity is to build new detectors. Some improvement can be made by increasing the impedance of the detectors, which will increase their responsivity and reduce the JFET contribution to the overall NEP ($\mathrm{NEP_{amp}}\sim R_0^{-0.5}$). However, high-impedance detectors can lead to increased microphonic noise. Reducing the bolometer lead conductance (G) or lowering the bath temperature (T) will reduce both thermal contribution ($\mathrm{NEP_{thermal}}\sim T^*G^{0.5}$) and amplifier contributions ($\mathrm{NEP_{amp}}\sim T^{0.5}*G^{0.5}$) to the NEP. Lowering the conductance of the bolometer leads reaches a limit of overloading the detector by the background. Reducing the bath temperature could be achieved by redoing the suspension of the refrigerator (see Sec. 2.2). We estimate such changes could improve the sensitivity by an order of magnitude.

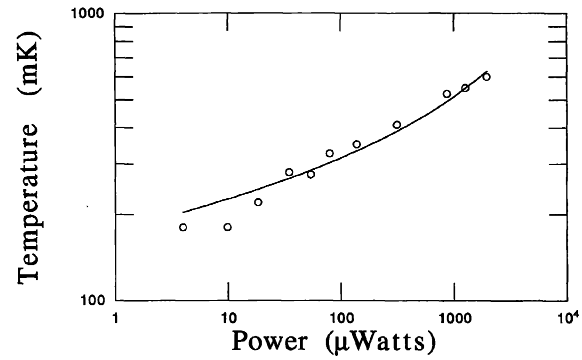

FIG. 4—Plot of equilibrium temperature vs. applied power for the cold stage of the ^{3}He system. The curve represents the best fit of Eq. (2). The fit gives $\epsilon=4.3\times10^{-4}\ \mu\mathrm{W}^{-1}$ and $n=1.9$, which implies $dN_{\rm adsorption}/dt\propto P^{0.5}$, where P is the ^{3}He pressure. The coldest temperature achieved is 180 mK without the heat load of the bolometer arrays. The operation temperature of 300 mK implies an added power of 100 μW to the cold stage.

Another way to improve the overall performance of the polarimeter is to increase the coupling constant (α) of the detectors (see Sec. 2.1). The NEFD scales as $\alpha^{-0.5}$ if the noise is due to photons and as α^{-1} if the noise is due to other sources (amplifier or thermal). Using larger detectors with dimensions that better match the 350 μm radiation or building composite detectors with better absorbtivity could produce significant improvements to our sensitivity.

3. SYSTEMATIC EFFECTS

Measurements of submillimeter polarization require accurate determination of systematic effects. In this section, we present measurements of the telescope and instrument polarization and their removal from the data. We describe measurements of the polarization modulation efficiency in the lab and at the CSO. We discuss the necessity for using dual arrays to remove slow atmospheric variations and we calculate systematic errors that can occur by failing to chop completely off an extended source.

3.1 Telescope and Instrument Polarization

To calibrate the polarimeter we performed a series of tests on the telescope. To measure the zero angle of the HWP we mounted a polarizing grid below the primary with the wires aligned along the elevation axis and performed polarization scans of OMC-1. We also made repeated polarization scans of Saturn, OMC-1, and the Moon to estimate the magnitude of the "edge effect" and to determine the telescope and instrument polarization.

TABLE 2
Detector Characteristics

Property	Value	Units
Electrical NEP:		
NEP_{photon} [a]	1.1×10^{-16}	Watts/$\sqrt{Hz}$
$NEP_{johnson}$[a]	2.3×10^{-16}	Watts/$\sqrt{Hz}$
$NEP_{thermal}$[a]	7.4×10^{-16}	Watts/$\sqrt{Hz}$
NEP_{load}[a]	0.1×10^{-16}	Watts/$\sqrt{Hz}$
$NEP_{amplifier}$[a]	6.3×10^{-16}	Watts/$\sqrt{Hz}$
Bolometers:		
Responsivity	4×10^{7}	Volts/Watt
Resistance	12	MΩ
Time Constant	2	mSec
Conductance	5×10^{-8}	Watt/K
Heat Capacity	10^{-10}	Joules/K

[a]Calculations and terminology from Mather (1982)

3.1.1 The Edge Effect

Gonatas et al. (1989) have analyzed the spurious polarization found in a single pixel-instrument when the image of a point source was offset toward the edge of a beam. This edge effect can be due to spatial nonuniformities in the polarization of the optics or from flux scattered into a beam. Such an effect has been noted for 1.3 mm (Novak et al. 1990) and for 800 μm (Minchin and Murray 1994) polarimeters. With Hertz, we have made repeated scans with a pixel centered on Saturn and at positions offset at half power points of the beam. The measurements at half power points agree with the polarization at the flux peak in position angle and in percent polarization within the errors (residuals$<2\sigma$, where σ is typically 1%–2%). Furthermore, we find that the signal in the wings (2 pixels away from Saturn's peak) has 5% of the peak signal. Thus it is unlikely that polarization from the wings of our beams affects the data.

3.1.2 The 1995 Data Analysis

For the 350 μm results, we performed a multiple linear regression, following Platt et al. (1991), to separate the source, telescope, and instrument polarization. This technique requires observations in sky tracking mode, fast 90 degree rotations, and pixel dithering to sort out the three components. For the standard analysis, we fit for an instrumental polarization for every pixel individually and a uniform telescope polarization across the array. The data consist of polarization scans of OMC-1 from three nights at two array settings; one centered at the infrared peak, KL, and the other centered 90″ to the south at the submillimeter peak, KHW (Keene et al. 1982). The fit to all the data gives a telescope polarization of 0.06±0.08% and an instrument polarization that varies across the array in a radial pattern that appears to increase with radius (shown in Fig. 5). The instrumental polarization in pixel 15 is 0.78±0.25% with an angle of 86±9 degrees, which is consistent with polarization scans on Saturn (assumed unpolarized).

The instrumental polarization is most likely due to the field lens. The field lens has a radius of curvature of 80 mm, and outer pixels are displaced by 13 mm from the lens axis. The expected polarization from the quartz lens (n=2.1) for outer pixels is 1% in the radial direction, which is in agreement with our measurements. The calculated and measured instrumental polarization have pixel-to-pixel variations less than 0.3%. Thus the standard analysis results in a negligible telescope polarization and an instrument polarization that varies with a radial pattern due to the quartz field lens and is subtracted in our analysis to better than 0.3%.

We note that analyzing the same data by different methods gives some discrepancies for overlapping points. By con-

TABLE 3
Performance Parameters

	1994	1995	Units
Wavelength	450	350	μm
Bandpass	61	37	μm
Polarization Modulation Efficiency	75	85	%
Operating Pixels	13	23	
NEFD	25	20	Jy/$\sqrt{Hz}$
Tmerit[a]	10.2	5.1	hours

[a]Defined by Equation 3.

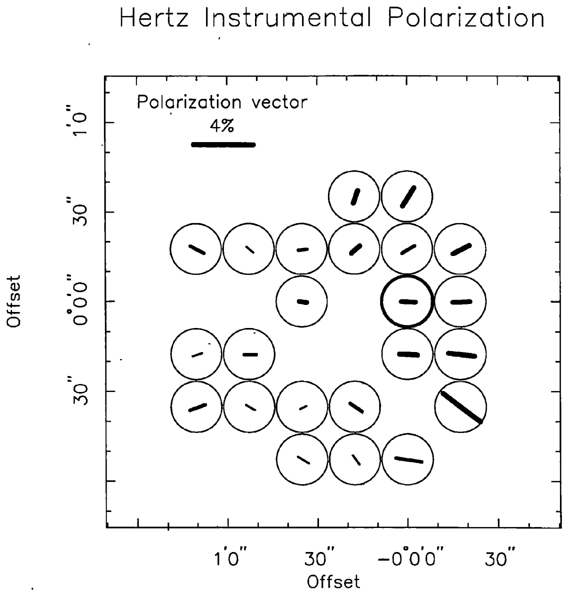

FIG. 5—Instrument polarization vectors derived from a multiple linear regression (see Sec. 3.1.2). Circles show the FWHM of the beam for each pixel. Missing pixels are due to high noise or wiring problems. Offsets are referenced from pixel 15 (shown as a darker circle). Thin, medium, and thick vectors show polarization vectors of 1σ, 2σ, and 3σ statistical significance, respectively. The polarization vectors indicate a radial pattern that increases in polarization with radius. The cause of this instrumental polarization is most likely due to the quartz field lens.

sidering the KL and KHW array settings as two separate datasets in the multiple linear regression, we can compare the results for overlapping sky positions. In all cases the differences for overlapping positions were less than 3σ; however, in all cases the KHW results had higher polarizations. Nevertheless, for all the overlapping points the position angles are extremely robust for both data-reduction analyses. Furthermore, trends in the data, such as decreasing polarization toward KHW, are seen with both methods.

This discrepancy is not likely due to a nonuniform polarization modulation efficiency (see Sec. 3.2) or flux from the reference beam (see Sec. 3.4). The most likely cause is a variation of the telescope polarization across the focal plane. The cassegrain relay optics of the CSO has five mirrors, two of which are flat steering mirrors at nearly 45 degrees. We have attempted to fit for such an effect by considering the telescope polarization for every pixel separately and get telescope polarizations as high as 1.8%, but with low statistical significance. The model is also flawed, because the rotation of the dewar with the sky will smear out focal-plane variations of the telescope polarization. Our dataset does not have sufficient signal to noise to model the telescope polarization, and the systematic effect can only be resolved with future tests at the telescope.

3.1.3 The 1994 Data Analysis

For the 1994 data, there were a number of differences in the instrument that factor into the data-reduction process. The instrument was filtered to match the 450 μm atmospheric window and to provide extra short wavelength blocking. We used a 6 mm HWP which we determined from lab tests to be too thick (see Sec. 3.2). During this initial observing run we had electronic problems that allowed use of only the top half of the array (13 detectors). Finally, these observations were made without an instrument rotator, which meant the instrument and telescope were at a fixed orientation to each other and that we could not observe in the sky-tracking or fast-rotation modes. The data were therefore binned into a grid on the sky as the array rotated around a source.

The rotation of the sky relative to the alt-az telescope during observations of OMC-1 and Saturn was sufficient to remove the combined instrument and telescope polarization (q_i, u_i) from the source polarization (q_s, u_s) for a central pixel (number 15) pointed at the peak of emission. The measured instrument polarization for pixel 15 was $P_{\text{instrument}} = 0.73\% \pm 0.12\%$ (systematic), which was subtracted uniformly for all pixels across the array. For pixels other than number 15, we used observations of the limb of the Moon to estimate the range of the instrument polarization ($\pm 0.35\%$).

Since the initial data reduction considered a uniform instrumental/telescope polarization across the array, we have reanalyzed the dataset using the telescope and instrument polarization derived from the 1995 data. These results are in good agreement with the standard 1994 analysis with no deviations greater than 2σ.

3.2 Polarization Modulation Efficiency

We have measured the modulation efficiency of Hertz in the lab and at the telescope for both the 450 and 350 μm configurations. For the lab measurements, we used a hot blackbody source and combinations of external grids. For the sky measurements, we observed Saturn, Orion, and the Moon with combinations of grids in front of the dewar window. We have determined the polarization modulation efficiency to be 75% for the 1994 data (450 μm) and 85% for the 1995 data (350 μm). All results have been corrected by this factor.

The modulation efficiency can be reduced from unity by an incorrect retardance at the operating wavelength, by a wide bandpass, or by an imperfect analyzing grid. For the 350 μm configuration, lab tests have determined that the 3.6 mm HWP gives the correct retardance. However, in the 450 μm configuration the HWP was too thick, which caused most of the modulation inefficiency. We calculate that the width of our passband ($\Delta\lambda/\lambda = 0.1$) should reduce the modulation efficiency by less than 2%. It is possible that a small light leak causes a reduction less than 5% for the 350 μm configuration; however, it is likely that the majority of the inefficiency is due to an imperfect polarizing grid. The polarization modulation efficiency is directly proportional to the grid efficiency which lab tests have determined to be $90 \pm 5\%$. Future improvements to the instrument will include higher quality free-standing wire grids with higher polarizing efficiency.

3.3 Dual Arrays

Atmospheric fluctuations cause variable attenuation of the signal ($e^{-\tau}$) especially for time scales longer than a few sec-

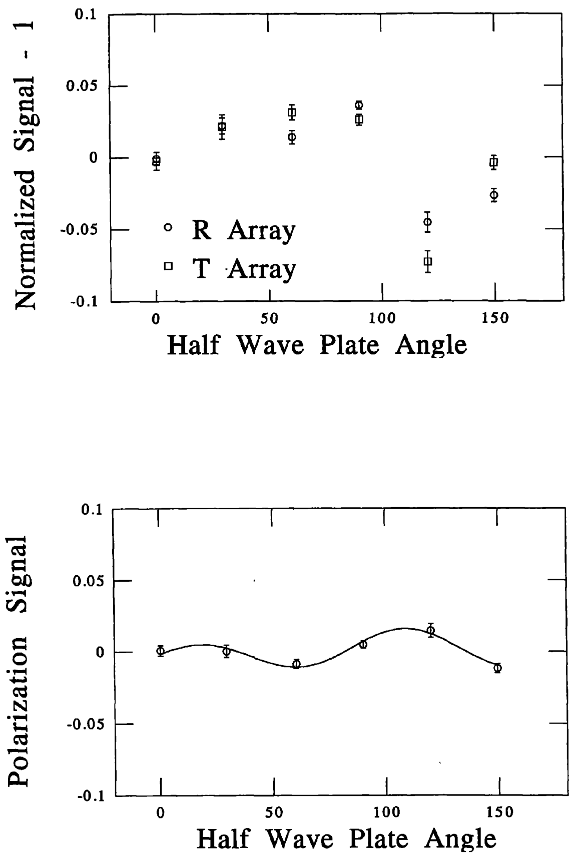

FIG. 6—Polarization data for a single file on OMC-1 (8 min of elapsed observing time). (a) Signals are normalized by the average signal to account for gain differences of the detectors and preamplifiers. The large correlated fluctuations, apparent at a HWP angle of 120°, are as great as 10% and are due to atmospheric variations. (b) The polarization signal $S(\Theta)$ [derived from Eq. (5)] of the same data is fit with both 90° and 180° components of the polarization signal. The large correlated fluctuation is effectively removed from the data. The 180° component is due to the HWP and does not affect our data analysis.

onds. This noise has a dramatic effect on the polarization signal of a single array since the HWP is stepped on the time scale of minutes. The fluctuations are uncorrelated with the position of the HWP; however, the low-frequency drifts are often large compared to the polarization signal. Simultaneous measurements with two arrays allow us remove this large noise contribution from the data.

Variations of the sky transmission with time will cause correlated fluctuations in the signals from two detectors (one from each array) observing the same position on the sky. On the other hand, a polarized source will produce anticorrelated signals in the two detectors with a periodicity of 90 degrees as the HWP is rotated. Figure 6(a) shows the signal for the normalized reflected (R) and transmitted (T) signals as a function of the HWP angle for an integration on Orion-KL during good weather conditions. The R and T signals are normalized to account for different amplifier gains. One can see that the R and T signals experience correlated fluctuations that are 10 times greater than the source polarization of 1% at KL.

The correlated noise due to the atmospheric attenuation is effectively removed by forming the polarization signal,

$$S(\theta)=\frac{R(\theta)e^{-\tau}-T(\theta)e^{-\tau}}{R(\theta)e^{-\tau}+T(\theta)e^{-\tau}}=\frac{R(\theta)-T(\theta)}{R(\theta)+T(\theta)}=A\cos[4(\theta-\phi)], \tag{5}$$

where θ is the position HWP, $e^{-\tau}$ is the atmospheric transmission, and A and ϕ are the magnitude and position angle of the polarization. In Fig. 6(b), we show the polarization signal for the same data. One can see that the atmospheric fluctuations have been removed and that a polarization signal can be fit to the data. We note that this fit also includes a 180 degree component, caused by reflections off the HWP, which does not affect our analysis.

To further test the importance of building a dual-array polarimeter, we have reduced the 1995 data for the R and T arrays separately as though they were single-array polarimeters. We find that the overall errors are higher by a factor of 2. The results also imply telescope and instrument polarizations that are not consistent with each other or to the polarizations from the standard analysis. This could be due to correlated noise across a single array that skews the multiple linear regression, which assumes that the measurement errors are uncorrelated.

We conclude that efficient polarimeters operating at submillimeter wavelengths require either dual arrays using a step and integrate strategy or rapid modulation of the HWP. The latter is not possible in the current system due to the microphonic noise inherent to bolometer detectors. However, rotating a vibrationless HWP continuously or using low-impedance detectors (less susceptible to microphonics) may provide an attractive solution in the future.

3.4 Reference Beam Flux

For submillimeter polarimetry, an unfortunate consequence of spatial chopping to remove the high sky background is the possibility of chopping into a reference beam with unknown flux and polarization. The problem is magnified by the empirical trend of increasing polarization with decreasing optical depth (Hildebrand et al. 1995). This trend can also be described as a broader distribution of polarized flux around flux peaks than the distribution of flux density. The problem of flux in the reference beam can be considerably reduced by spatially chopping well-off flux peaks. However, even with the large spatial chop available at the CSO (6′–8′), we still must consider the possibility of reference beam flux affecting the results.

To calculate this systematic effect, we wish to compare the measured polarized and total flux to an estimate of the polarized and total flux from the reference beam. Consider a source position whose polarization is described by the normalized Stokes parameters

$$q_s=P_s\cos(2\phi_s), \tag{6}$$

$$u_s=P_s\sin(2\phi_s), \tag{7}$$

TABLE 4
350 μm Polarization Results

ΔRA[a]	ΔDEC[a]	P(%)	σ_P[b]	ΔP_+[c]	ΔP_-[c]	Φ(°)	σ_Φ[b]	$\Delta\Phi$[c]
14	-94	2.4	0.7	+0.3	-0.5	24.1	8.4	4.4
35	-61	4.1	1.2	+0.6	-1.6	18.1	8.4	9.2
20	-70	6.8	2.0	+0.2	-1.2	29.3	8.2	3.2
5	-79	2.6	0.5	+0.2	-0.4	23.8	6.1	3.3
-11	-87	2.4	0.4	+0.2	-0.4	25.7	5.2	3.4
26	-46	4.4	0.7	+0.5	-1.3	33.3	4.3	6.5
11	-55	4.1	0.6	+0.3	-0.8	22.6	4.1	4.2
-4	-63	2.6	0.6	+0.3	-0.5	24.4	6.7	4.1
-19	-72	2.8	0.6	+0.3	-0.6	27.0	5.7	4.8
-35	-81	3.2	0.8	+0.5	-1.0	22.0	7.5	7.4
48	-13	3.6	1.1	+0.7	-1.6	31.5	8.8	10.6
33	-22	3.2	0.5	+0.6	-1.2	24.7	4.7	9.0
18	-30	3.4	0.5	+0.4	-1.0	31.3	4.3	6.3
2	-39	3.7	0.7	+0.3	-0.8	20.9	5.0	4.6
-13	-48	4.0	0.4	+0.3	-0.7	21.8	3.1	3.4
-28	-57	2.7	0.5	+0.7	-1.3	23.4	5.6	12.1
-43	-66	3.1	0.8	+0.4	-0.8	33.3	7.3	6.0
39	2	3.7	0.9	+0.5	-1.3	18.7	6.9	7.8
24	-6	2.9	0.4	+0.3	-0.6	24.8	3.5	4.7
9	-15	3.2	0.3	+0.1	-0.2	34.0	2.3	1.6
-6	-24	3.8	0.3	+0.2	-0.4	27.7	1.9	2.3
-22	-33	3.9	0.4	+0.3	-0.8	28.7	2.8	4.5
-37	-42	3.1	0.8	+0.6	-1.2	22.6	7.9	9.5
-52	-50	3.8	1.3	+0.8	-2.0	36.1	9.5	13.3
46	26	2.8	1.0	+0.5	-1.0	15.5	9.8	8.4
30	18	2.4	0.7	+0.3	-0.5	21.9	8.1	4.5
15	9	2.1	0.3	+0.2	-0.3	28.9	3.7	3.2
0	0	1.4	0.1	+0.1	-0.1	32.0	2.4	1.9
-15	-9	2.7	0.4	+0.2	-0.4	25.4	4.3	3.1
-30	-18	4.1	0.6	+0.4	-1.0	30.8	4.1	5.2
-46	-26	4.6	0.7	+0.5	-1.5	26.4	4.5	7.0
37	42	3.1	1.0	+0.4	-0.8	15.0	9.6	5.7
22	33	2.5	0.4	+0.2	-0.3	21.5	4.0	2.6
6	24	1.6	0.3	+0.2	-0.3	38.4	4.7	4.2
-24	6	4.0	0.6	+0.3	-0.6	28.2	4.0	3.4
-39	-2	3.9	0.6	+0.5	-1.3	30.8	4.3	7.4
-55	-11	4.4	0.9	+0.5	-1.5	25.6	5.9	7.4
13	48	2.2	0.6	+0.4	-0.7	32.8	7.3	8.0
-2	39	2.4	0.4	+0.4	-0.7	40.9	5.3	7.2
-18	30	3.3	0.4	+0.4	-0.8	40.5	3.1	5.2
-33	22	3.1	0.5	+0.6	-1.2	43.1	4.6	9.5
-48	13	2.8	0.8	+0.8	-1.5	36.6	8.5	13.9
-63	4	3.8	1.1	+0.9	-2.1	56.6	8.5	14.0
-11	55	2.4	0.5	+0.7	-1.1	36.4	6.4	12.5
-26	46	2.7	0.6	+0.6	-1.2	46.3	5.9	10.9
-42	37	3.6	0.9	+0.7	-1.6	44.0	7.0	10.5
-57	28	4.9	1.2	+0.7	-2.3	38.4	6.9	10.8

[a] Sky positions are offset in arcsec from the submillimeter flux peak, KL, in Epoch 1950 coordinates (α=5h32m47.02s, δ=-5°24'25.3, Wright et al. (1992))
[b] Statistical Errors
[c] Systematic Errors due to flux in the reference beam (see section 3.4)

and intensity (I_s). The reference beam will have similar Stokes parameters (q_r, u_r) and intensity (I_r). The polarimeter measures an apparent intensity ($I_a = I_s - I_r$) and polarization

$$q_a = \frac{I_s q_s - I_r q_r}{I_s - I_r}, \tag{8}$$

$$u_a = \frac{I_s u_s - I_r u_r}{I_s - I_r}. \tag{9}$$

To simplify the above relations we define the ratios

$$V = \frac{P_r}{P_a} \tag{10}$$

and

$$Y = \frac{I_s}{I_r} \tag{11}$$

to make an estimate of the expected polarization error. If we rotate our frame of reference such that $\phi_a = 0$ and thus $u_a = 0$, and combine Eqs. (6)–(11), we find that the source polarization is given by

$$P_s = P_a \frac{1}{Y} \sqrt{(Y-1)^2 + V^2 + 2(Y-1)V\cos(2\phi_r)}, \tag{12}$$

$$\phi_s = \frac{1}{2}\,\mathrm{Arctan}\left(\frac{V\sin(2\phi_r)}{Y-1+V\cos(2\phi_r)}\right). \tag{13}$$

TABLE 5
450 μm Polarization Results

ΔRA[a]	ΔDEC[a]	P(%)	σ_p[b]	ΔP_+[c]	ΔP_-[c]	Φ(°)	σ_Φ[b]	$\Delta\Phi$[c]
18	18	3.2	0.4	+0.1	-0.3	38.1	4.2	2.1
18	0	1.9	0.4	+0.2	-0.3	32.3	6.9	3.5
18	-18	1.4	0.5	+0.5	-0.7	32.7	9.7	12.8
18	-35	4.5	1.0	+0.5	-1.3	37.5	6.3	6.5
18	-53	4.7	1.5	+0.4	-1.4	35.6	9.1	6.1
0	0	1.1	0.2	+0.1	-0.1	33.4	5.0	2.5
0	-18	2.0	0.5	+0.2	-0.3	6.8	5.9	3.4
0	-35	4.4	0.5	+0.2	-0.7	24.7	3.4	3.1
0	-53	5.8	1.6	+0.1	-0.6	19.8	7.9	1.8
-18	-35	3.1	0.7	+0.2	-0.4	25.6	6.2	2.7
-18	-70	3.9	0.9	+0.2	-0.5	30.4	6.6	2.8
-35	0	4.5	1.0	+0.4	-1.1	31.0	6.0	4.9
-35	-18	3.5	1.0	+0.4	-1.0	29.3	7.8	6.4
-35	-35	4.8	1.1	+0.3	-1.1	18.4	6.8	4.7
8	-72	3.5	0.6	+0.3	-0.6	37.7	5.1	3.9
8	-90	3.3	0.6	+0.2	-0.5	49.0	5.6	3.3
8	-125	7.5	2.1	+0.2	-2.6	48.6	7.9	6.6
-10	-72	2.5	0.5	+0.2	-0.4	25.4	6.0	3.4
-10	-90	2.1	0.3	+0.2	-0.3	28.3	4.2	3.1

[a] Sky positions are offset in arcsec from the submillimeter flux peak, KL, in Epoch 1950 coordinates (α=5h32m47.02s, δ=-5°24'25.3, Wright et al. (1992))
[b] Statistical Errors
[c] Systematic Errors due to flux in the reference beam (see section 3.4)

Since we have no knowledge of the direction of the polarization in the reference beam we maximize and minimize Eqs. (12) and (13), with respect to ϕ_r, to derive

$$\Delta P_{\text{sys}}^{+}=P_a\left(\frac{V-1}{Y}\right), \tag{14}$$

$$\Delta P_{\text{sys}}^{-}=P_a\left(\frac{V+1}{Y}\right), \tag{15}$$

$$\Delta\phi_{\text{sys}}=\frac{1}{2}\,\text{Arctan}\left[\left(\frac{Y-1}{V}\right)^2-1\right]^{-1/2} \tag{16}$$

where $P_s=P_{a\,-\Delta P_{\text{sys}}^{-}}^{\,+\Delta P_{\text{sys}}^{+}}\pm\sigma_p$ (statistical) and $\phi_s=\phi_a\pm\Delta\phi_{\text{sys}}$ $\pm\sigma_\phi$ (statistical).

We derive an upper limit to the errors by assuming the reference beam polarization is equal to the maximum polarization (9%) observed at 100 μm (Hildebrand et al. 1995). One can estimate the value for Y by comparing the flux at source and reference beam positions from large-scale photometric maps. At best this is an estimate because published photometric maps that cover an area including the reference beam position usually sample with larger beams.

For large values of Y, Eqs. (14)–(16) go to zero; however where Y has values <10, the systematic error can be larger than the statistical error. For example, consider the peak of OMC-1 (KL) and the position with the largest systematic errors (ΔRA$=-63$; ΔDEC$=4$, in Table 4). At the KL peak, the ratio of the source flux to the reference flux is at least 100 and the ratio of the largest possible polarization in the reference beam to the apparent polarization is 7.7. With these estimates the systematic errors are $\Delta P_{\text{sys}}^{+}<0.1\%$, $|\Delta P_{\text{sys}}^{-}|$ $<0.1\%$, and $\Delta\phi<1.^{\circ}9$. The worst-case example has estimated reference beam values of $V=2.4$ and $Y=6$, which give systematic errors of $\Delta P_{\text{sys}}^{+}<0.9\%$, $|\Delta P_{\text{sys}}^{-}|<2.1\%$, and $\Delta\phi_{\text{sys}}<14°$, which can be compared to the statistical errors of $\sigma_{p\text{stat}}=1.1\%$, and $\sigma_{\phi\text{stat}}=9°$. We have estimated this systematic error separately for all the measurements presented in Sec. 4.

To further check the OMC-1 data against systematic effects, we have broken the data with the array centered at KL into two sets: one chopping perpendicular to the ridge and one chopping within 20° of the extended ridge flux. For all overlapping points between the datasets, the results are consistent to within the statistical errors. Thus our estimate of the reference beam systematic error can be viewed as a cautious upper limit.

4. RESULTS

During an initial engineering run at the CSO in Fall of 1994, we tested Hertz, the chopping secondary mirror (constructed at the University of Chicago), and the telescope interface. During this run we obtained 19 3σ measurements for OMC-1 at 450 μm. In Fall of 1995, we observed OMC-1 at 350 μm with an upgraded instrument and improved telescope facilities and obtained 46 3σ measurements. The data for both years are given in Tables 4 and 5. Maps showing the flux density and polarization vectors are shown in Fig. 7.

The 450 μm data were taken 1994 October 23–26. The 350 μm data were taken 1995 Oct. 30–Nov. 1. Observing conditions were excellent for the 1994 observations with an average radiometer optical depth (225 GHz) of 0.06. The weather conditions in 1995 were considerably worse with only 3 out of 14 nights adequate for observing at 350 μm. However, during those three nights the conditions were good with an average radiometer optical depth of 0.06. The improved instrument and higher signal at 350 μm resulted in a larger number of detections for the 1995 data.

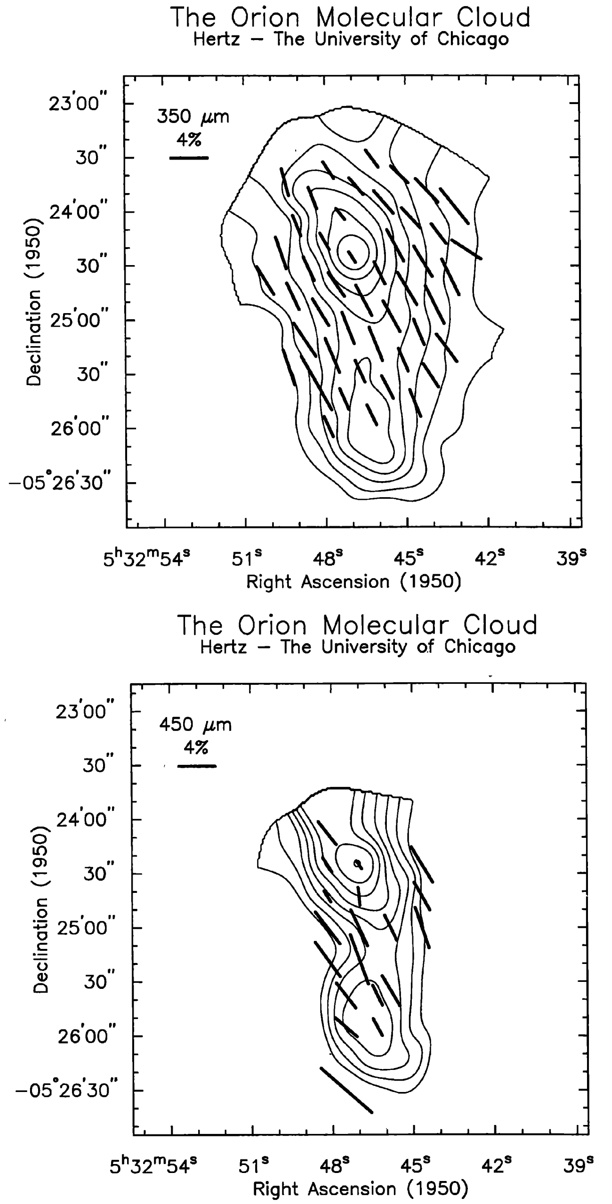

FIG. 7—Polarization maps of Orion (OMC-1) at 350 and 450 μm. The contours trace the flux density, and vectors represent the polarization. A 4% polarization vector is shown in the upper left of both figures. All plotted E vectors are of 3σ significance above the statistical noise. (a) The 350 μm polarization measurements taken in Fall of 1995. Contours levels are at 0.16, 0.20, 0.25, 0.32, 0.40, 0.50, 0.63, 0.79, and 1.0 times the peak flux of 1800 Jy. (b) The 450 μm measurements taken in Fall of 1994. Contour levels at 0.16, 0.20, 0.25, 0.32, 0.40, 0.50, 0.63, 0.79, and 1.0 times the peak flux of 600 Jy.

The 350 and 450 μm measurements constitute the largest maps of submillimeter polarization to date. The polarization angles agree well with previous measurements in the submillimeter (Flett and Murray 1991) and millimeter (Leach et al. 1991) as well as with lower-resolution 100 μm results (Hildebrand et al. 1995). The photometric maps made with the same instrument agree well with previous published photometric maps in the submillimeter (Keene et al. 1982) and millimeter (Mezger et al. 1990). The cold dust sampled at 350 μm appears to have the same polarization features around the KL peak as seen at 100 μm, namely, large-scale pinching and systematic reduction of polarization with optical depth (Schleuning 1997).

5. SUMMARY AND FUTURE IMPROVEMENTS

We have constructed a submillimeter polarimeter for operation at the Caltech Submillimeter Observatory. The optical, cryogenic, and electrical components provide the capability to make scores of polarization measurements for bright sources. We have tested the polarimeter to determine the telescope and instrument polarizations and have removed their effects from the data where possible. The systematic effect due to polarized flux in the reference beams has been estimated. Observations in the Fall of 1994 and 1995 have produced 19 (450 μm) and 46 (350 μm) 3σ detections of polarization in OMC-1.

The polarimeter, while operational and capable of significant scientific observations, can be improved in a number of areas. The polarization modulation efficiency can be increased by higher-quality free-standing wire grids. Antireflection coating the lenses will increase the throughput and reduce the instrumental polarization. The sensitivity can be greatly improved with higher-responsivity bolometers and a lower bath temperature. Such improvements would reduce the instrumental systematic effects and improve the sensitivity by an order of magnitude.

We thank D. Pernic, A. Barth, S. Dayton, S. Knudsen, T. Keidl, R. J. Pernic, J. Sundwall, C. Wirth, and the staff of the Caltech Submillimeter Observatory for help with preparation of the instrument and observations. We are grateful for many useful discussions with J. A. Davidson, M. Dragovan, J. L. Dotson, and R. F. Loewenstein. This work was supported by NASA Grant No. NSG 2057 and by NSF Grant No. AST 8917950. The Caltech Submillimeter Observatory is funded by the NSF through Contract No. AST 9313929. Two of the authors (D.A.S. and C.D.D) were supported by NASA Graduate Student Researchers Program Grants No. NGT-51311 and No. NGT-50894.

REFERENCES

Dotson, J. L. 1996, ApJ, 470, 566
Flett, A. M., and Murray, A. G. 1991, MNRAS, 249, 4
Gonatas, D. P., Wu, X. D., Novak, G., and Hildebrand, R. H. 1989, Appl. Opt., 28, 1000
Hildebrand, R. H. 1986, Opt. Engineering, 25, 323
Hildebrand, R. H. 1988, QJRAS, 29, 327
Hildebrand, R. H., Davidson, J. A., Dotson, J., Figer, D. F., Novak, G., Platt, S. R., and Tao, L. 1993, ApJ, 417, 565
Hildebrand, R. H., Dotson, J. L., Dowell, C. D., Platt, S. R., Schleuning, D., Davidson, J. A., and Novak, G. 1995, in Proceedings of the Airborne Astronomy Symposium on the Galactic Ecosystem: From Gas to Stars to Dust, ed. M. R. Haas, J. A. Davidson, and E. F. Erickson (San Francisco, ASP), p. 97.
Keene, J., Hildebrand, R. H., and Whitcomb, S. E. 1982, ApJ, 252, L11

Leach, R. W., Clemens, D. P., Kane, B. D., and Barvainis, R. 1991, ApJ, 370, 257

Loewenstein, E. V., Smith, D. R., and Morgan, R. L. 1973, Appl. Opt., 12, 398

Mather, J. C. 1982, Appl. Opt., 21, 1125

Mezger, P. G., Wink, J. E., and Zylka, R. 1990, A&A, 228, 95

Minchin, N. R., and Murray, A. G. 1994, A&A, 286, 579

Morris, M., Davidson, J. A., Werner, M., Doton, J., Figer, D. F., Hildebrand, R., Novak, G., and Platt, S. R. 1992, ApJ, 399, L63

Murray, A. G., Flett, A. M., Murray, G., and Ade, P. R. 1992, Infrared Phys., 33, 113

Novak, G., Gonatas, D. P., Hildebrand, R. H., and Platt, S. R. 1989, PASP, 101, 215

Novak, G., Dotson, J. L., Dowell, C. D., Goldsmith, P. F., Hildebrand, R. H., Platt, S. R., and Schleuning, D. A. 1997, ApJ (submitted)

Novak, G., Predmore, C. R., and Goldsmith, P. F. 1990, ApJ, 355, 166

Platt, S. R., Hildebrand, R. H., Pernic, R. J., Davidson, J. A., and Novak, G. 1991, PASP, 103, 1193

Schleuning, D. A., Dowell, C. D., and Platt, S. R. 1996, in Polarimetry of the Interstellar Medium, ed. W. G. Roberge and D. C. Whittet, ASP Conference Series (San Francisco, ASP), p. 285

Schleuning, D. A. 1997, Ph.D. thesis (in preparation)

Wang, N., et al. 1996, Appl. Opt. 35, 6629

White, G. K. 1993, Experimental Techniques in Low-Temperature Physics, 3rd Edition (New York, Oxford University Press)

Wright, M., Sandell, G., Wilner, D. J., and Plambeck, R. L. 1992, ApJ, 393, 225